

NATIONAL INSTITUTE FOR FUSION SCIENCE

Zonal Flows and Ion Temperature Gradient Instabilities  
in Multiple-helicity Magnetic Fields

S. Ferrando-Margalet, H. Sugama, T.-H. Watanabe

(Received - July 19, 2007 )

NIFS-878

Aug. 2007

RESEARCH REPORT  
NIFS Series

This report was prepared as a preprint of work performed as a collaboration research of the National Institute for Fusion Science (NIFS) of Japan. The views presented here are solely those of the authors. This document is intended for information only and may be published in a journal after some rearrangement of its contents in the future.

Inquiries about copyright should be addressed to the Research Information Office, National Institute for Fusion Science, Oroshi-cho, Toki-shi, Gifu-ken 509-5292 Japan.

E-mail: [bunken@nifs.ac.jp](mailto:bunken@nifs.ac.jp)

**<Notice about photocopying>**

In order to photocopy any work from this publication, you or your organization must obtain permission from the following organization which has been delegated for copyright for clearance by the copyright owner of this publication.

Except in the USA

Japan Academic Association for Copyright Clearance (JAACC)  
6-41 Akasaka 9-chome, Minato-ku, Tokyo 107-0052 Japan  
Phone: 81-3-3475-5618 FAX: 81-3-3475-5619 E-mail: [jaacc@mtd.biglobe.ne.jp](mailto:jaacc@mtd.biglobe.ne.jp)

In the USA

Copyright Clearance Center, Inc.  
222 Rosewood Drive, Danvers, MA 01923 USA  
Phone: 1-978-750-8400 FAX: 1-978-646-8600

# Zonal flows and ion temperature gradient instabilities in multiple-helicity magnetic fields

S. Ferrando-Margalet<sup>1</sup>, H. Sugama<sup>1,2</sup>, T.-H. Watanabe<sup>1,2</sup>

<sup>1</sup> *National Institute for Fusion Science, Toki 509-5292, Japan*

<sup>2</sup> *The Graduate University for Advanced Studies, Toki 509-5292, Japan*

## Abstract

Effects of multiple-helicity magnetic fields on the ion temperature gradient (ITG) instability and on the zonal flow (ZF) evolution are studied with the linear gyrokinetic Vlasov code GKV. The model helical fields corresponding to the standard and inward-shifted axis configurations of the Large Helical Device are used to investigate how ITG mode properties and ZF evolution response to a given source are influenced by the field geometry. It is shown that, in the inward-shifted configuration, the ITG mode growth rate increases slightly while the ZF is sustained for a longer time. In addition, velocity-space structures of the ion perturbed distribution function are numerically obtained which illustrate the validity of the analytical prediction that the plasma inward shift retards the radial drift of the helically trapped particles leading to the enhancement of the ZF response. This supports the conjecture that anomalous transport can be reduced by the ZF generated in the configurations optimized to decrease the neoclassical transport.

## I. INTRODUCTION

Helical magnetic plasma confinement systems are more influenced by neoclassical transport (NCT) than tokamaks because of their lack of axisymmetry. This is why NCT optimization is one of the main concerns towards the realization of fusion in nonaxisymmetric devices [1]. Several approaches have been proposed in order to reduce the transport in helical systems and a number of new experiments have been devised [2–6], some of them presently under construction. Recent experimental results [7] seem to suggest that there exists a correlation between NCT optimization and reduction of turbulent or anomalous transport (AT) which is also becoming a major issue towards the characterization of transport-optimized experiments [8–10].

It is well-known, and it has been observed both in laboratory and in nature, that turbulent behavior often self-organizes into a stream-like flow called the Zonal Flow (ZF) [11–13]. In plasma fusion experiments, the importance of the ZF lies on the fact that it tends to reduce the AT. The ZF evolution is governed by the non-linear interaction with the drift waves (which eventually determine the turbulence behavior), as well as by the linear damping process through collisions and collision-less mechanisms such as the Landau damping. It has been shown in the past [8, 9, 14] that linear studies of the ZF behavior can provide important information as to its dependence magnetic geometry which can help to develop ways to utilize the ZF capacity to reduce the AT in magnetically confined plasmas.

The original motivation of the present work comes from a set of experiments in the Large Helical Device (LHD) [15] in which the magnetic configuration was shifted inwards by means of a vertical field [7]. In LHD, inward shifted configurations are known to reduce the neoclassical helical ripple transport [16]. These experiments, however, showed a reduction, not only of the NCT, but also of the AT. We expect that the decrease in AT is achieved through the enhancement of the ZF caused by the slower radial drift of helically trapped particles in the inward shifted configuration. The results presented here are intended to identify the causes by which the change in magnetic geometry due to

the inward shift contribute to the enhancement of the ZF and reduction of the AT, thus highlighting the correlation between the optimizations of NCT and AT. This is done by first studying the change on the ion temperature gradient (ITG) mode destabilization, which represents the source of the turbulence, and then investigating the ZF evolution both in standard and in inward shifted configurations.

The calculations shown here have been performed with the GKV code [17] utilized in the past to simulate ZF, geodesic acoustic modes (GAM) and ITG destabilization in tokamaks and helical systems with single helicity magnetic fields. In addition, nonlinear simulations with simple multiple-helicity fields to model LHD's inward shifted-axis configurations have been recently carried out [10]. In the present work, we extend the calculations on shifted LHD configurations with the inclusion of more accurate values in the description of the magnetic field. From the comparison between the simple and the more realistic models, we aim to identify which parameters are more influential to the AT optimization achieved in the shifted-axis LHD scenarios as observed in the experiment.

The GKV code solves the gyrokinetic equation of the perturbed ion gyrocenter distribution function for the electrostatic case [8, 17, 18],

$$\frac{\partial \delta f}{\partial t} + v_{\parallel} \mathbf{b} \cdot \nabla \delta f + \frac{c}{B_0} (\mathbf{b} \times \nabla \Phi \cdot \nabla \delta f) + \mathbf{v}_d \cdot \nabla \delta f - \mu (\mathbf{b} \cdot \nabla \Omega) \frac{\partial \delta f}{\partial v_{\parallel}} = (\mathbf{v}_* - \mathbf{v}_d - v_{\parallel} \mathbf{b}) \cdot \frac{e \nabla \Phi}{T_i} F_M + C(\delta f), \quad (1)$$

and the quasineutrality condition with adiabatic electron response,

$$\int J_0 \delta f_{k_x, k_y} d^3 v - \frac{e \phi_{k_x, k_y}}{T_i} n_0 (1 - \Gamma_0) = \delta n_{e, k_x, k_y}, \quad (2)$$

where  $\delta f_{k_x, k_y}$  and  $\delta n_{e, k_x, k_y}$  are the Fourier components of  $\delta f$  and  $\delta n_e$ , respectively. Here,  $\Gamma_0 = e^{-b} I_0(b)$ , with  $b = (k_{\perp} v_{ti} / \Omega_i)^2$ ,  $J_0$  is the zeroth order Bessel function and  $I_0$  is the modified zeroth order Bessel function. The electron density fluctuation is assumed to be given by:

$$\delta n_{e, k_x, k_y} = \begin{cases} n_0 e(\phi_{k_x, k_y} - \langle \phi_{k_x, k_y} \rangle) / T_e & \text{if } k_y = 0 \\ n_0 e \phi_{k_x, k_y} / T_e & \text{if } k_y \neq 0, \end{cases}$$

where  $n_0$  is the averaged electron density (see Ref. [10] for more details on the notation).

We consider ITG modes as the source of the turbulence. ZFs are generated by the ITG turbulence but, simultaneously, they regulate it. Linear calculations can not give information about nonlinear saturation levels of the turbulence but, in turn, they do not require huge computer resources, allowing the survey of different scenarios for a wider range of parameters, from which some important cases can be selected for further investigation by non-linear simulations. In particular, linear calculations can be very useful in comparing effects of magnetic geometry on ITG mode destabilization and on ZF response to a given source. In the following sections, these type of comparative studies are applied to the standard and inward-shifted LHD configurations.

The remainder of the paper is organized as follows. Section II defines the modeling of the standard and inward-shifted LHD configurations in terms of the Fourier representation of the magnetic field strength. Section III presents linear ITG instability simulation results for both configurations emphasizing on a proper choice of parameters for the calculation relevant to experimental conditions. Finally, Sec. IV is devoted to the linear simulation and analysis of the ZF for both scenarios. A discussion of the results follows in the conclusion.

## II. MULTIPLE-HELICITY CONFIGURATIONS

The standard and shifted LHD configurations can be modeled by a Fourier expansion of the magnetic field strength that includes a toroidal term  $\epsilon_t$ , a main helicity term  $\epsilon_h = \epsilon_L$  and side-band terms  $\epsilon_+ = \epsilon_{L+1}$  and  $\epsilon_- = \epsilon_{L-1}$ :

$$\begin{aligned} B/B_0 &= 1 - \epsilon_{00} - \epsilon_t \cos(\theta) - \sum_{l=L-1}^{L+1} \epsilon_l \cos[(l - Mq)\theta - M\alpha] \\ &= 1 - \epsilon_T(\theta) - \epsilon_H(\theta) \cos[(L - Mq)\theta - M\alpha] + \chi_H(\theta), \end{aligned} \quad (3)$$

where

$$\begin{aligned} \epsilon_T(\theta) &= \epsilon_t \cos(\theta), & C(\theta) &= \sum_{l=L-1}^{L+1} \epsilon_l \cos(l\theta), \\ \epsilon_H(\theta) &= \sqrt{C^2(\theta) + D^2(\theta)}, & D(\theta) &= \sum_{l=L-1}^{L+1} \epsilon_l \sin(l\theta), \\ \chi_H(\theta) &= \arctan[D(\theta)/C(\theta)]. \end{aligned}$$

Here,  $\theta$  ( $\zeta$ ) is the poloidal (toroidal) angle and  $M$  ( $L$ ) is the toroidal (main poloidal) period number of the field. For the LHD, we use  $L = 2$  and  $M = 10$ . The magnetic shear is denoted by  $\hat{s}$ ,  $q$  is the safety factor and  $\alpha = \zeta - q\theta$  is the label of the magnetic field line. The effect of the multiple helicity terms is included in the functions  $\epsilon_H(\theta)$  and  $\chi_H(\theta)$ .

The stability of the ITG modes depends in great measure on the magnetic drift frequency which is defined as  $\omega_d = \mathbf{k}_\perp \cdot \mathbf{v}_d = -(k_\theta G_c(\theta)/R_0\Omega)(v_\parallel^2 + v_\perp^2/2)$ . Here,  $G_c(\theta)$  describes the curvature along the field line is defined by  $G_c(\theta) = -(R_0/k_\theta)(\mathbf{k}_\perp \times \mathbf{b}) \cdot (\nabla B/B)$ . Therefore, multiple helicity terms alter the shape of  $G_c(\theta)$  as follows:

$$\begin{aligned} G_c &= \frac{R_0\epsilon_t}{r} \left[ \frac{r \epsilon'_{00}}{\epsilon_t} + \left( \frac{r \epsilon'_t}{\epsilon_t} \right) \cos \theta + \hat{s} \theta \sin \theta \right. \\ &\quad \left. + \sum_{l=L-1}^{L+1} \left\{ \left( \frac{r \epsilon'_l}{\epsilon_t} \right) \cos [(l - Mq_0)\theta - M\alpha] + \left( \frac{\epsilon_l}{\epsilon_t} \right) \hat{s} \theta l \sin [(l - Mq_0)\theta - M\alpha] \right\} \right], \end{aligned} \quad (4)$$

where  $\epsilon'_{00}$  represents the averaged normal curvature [19].

Here, the flux tube coordinates [20] have been used in a similar way as in [10], *i.e.*,  $x = r - r_0$ ,  $y = (r_0/q_0)[q(r)\theta - \zeta]$  and  $z = \theta$ , with  $R_0$  and  $r$  being the major and minor radii, respectively;  $q(r)$  is the safety factor and  $\hat{s} \equiv (r_0/q_0)dq/dr$  is the magnetic shear. In order to model the standard and inward-shifted LHD configurations, two different sets of implementations of magnetic parameters have been considered. The first one consists of idealized versions of the standard and inward-shifted axis configurations, both with the same values for the safety factor and the magnetic shear namely  $q = 1.5$  and  $\hat{s} = -1$ . In addition, the radial dependence of the expansion amplitudes are assumed to follow  $\epsilon_l \propto r^l$  based on the large aspect ratio (or cylindrical) representation, and we impose  $\epsilon_t = r/R_0$  as in [9, 10]. Under these conditions, the standard case is chosen to be a pure single helicity case, with side-band coefficients imposed to zero. The inward-shifted case's coefficients, in turn, are chosen so that they give a high NCT optimization following [21].

Hereafter, these configurations are referred to as Standard-A (*S-A*) and Inward-A (*I-A*), respectively. The other set of model configurations are implemented with more realistic values for the magnetic field coefficients, their radial derivatives,  $q$  and  $\hat{s}$  which are taken from the vacuum magnetic field (the use of vacuum field data is justified because we consider here low beta plasmas only). We use the terms Standard-B (*S-B*) and Inward-B (*I-B*) to refer to this set in the remainder of the paper. The values for both sets are shown in Table I.

In Fig.1, profiles for the normalized magnetic field strength along a magnetic field line for the *S-A/I-A* set and the *S-B/I-B* set implementations, respectively, are displayed in the top row. The two bottom plots correspond to the profiles of  $G_c$ . A fair amount of qualitative information can be already drawn from Fig.1. The magnetic field strength profile in *S-B* slightly deviates from the pure single helicity case *S-A* and the wells become deeper away from  $\theta = 0$  while becoming shallower around this point. There is an increase of the number of helical ripples in the realistic set-up due to the higher safety factors of *S-B* and *I-B*. For *I-A* and *I-B*, the ripples of the magnetic field strength show almost constant values at their bottoms, which implies that the radial drift of deeply trapped particles is weak and the NCT is small in the inward shifted configurations. The curvature factor  $G_c$  provides a very good intuitive picture of how unfavorable the curvature is with respect to the stability of the ITG modes (see Ref. [21]), *i.e.*,  $G_c > 0$  around  $\theta = 0$  is destabilizing while  $G_c < 0$  is stabilizing. From the  $G_c$  profiles in Fig.1 it is clear that, while there is a considerable difference between *S-A* and *I-A* profiles around  $\theta = 0$ , the discrepancy is very small between the *I-B* and *S-B* cases. In addition, the latter ones are more clearly positive than the former ones. It is, thus, reasonable to expect a greater difference in the growth rates of the unstable modes in the simple models (*S-A*, *I-A*) than in the more realistic models (*S-B*, *I-B*), with possibly higher growth rates in the latter ones. The ITG instability for both sets of configurations is examined in greater detail in the next section.

### III. LINEAR ITG STABILITY

Linear gyrokinetic Vlasov simulations have been carried out in a similar way as in [10, 17] but with the implementation of the multiple helicity terms described in Sec. II to study the behavior of the unstable ITG modes. Other parameters used in the simulations are  $L_n/R_0 = 0.3$ ,  $\eta_i = L_n/L_T = 4$ ,  $T_e/T_i = 1$  and  $\alpha = 0$ , where  $L_n$  and  $L_T$  represent scale lengths of the averaged density and temperature gradients, respectively. In both sets of scenarios, the same initial perturbation is imposed triggering the growth of the unstable modes for various values of  $k_y \rho_{ti}$  (where  $\rho_{ti}$  is the thermal ion gyroradius radius defined as  $\rho_{ti} = v_{ti}/\Omega_i$  with  $v_{ti} = \sqrt{T_i/m_i}$ ). Their growth rates and the real frequencies are depicted in Fig.2. Here, the real frequencies  $\omega_r$  and the growth rates  $\gamma$  have the units  $v_{ti}/L_n$ . The left hand side picture shows a remarkable difference between the simple model configurations (*S-A* and *I-A*), which is in agreement with the qualitative discussion stated before in Sec. II. On the right hand side picture, growth rates and real frequencies for the more realistic models (*S-B* and *I-B*) are displayed. The growth rates are higher than in the simple models and, indeed, they are very similar between each other, also confirming the predictions made from examining the geometric factor profiles in the previous section. This behavior of the ITG modes has been successfully benchmarked with eigenvalue analysis results of the GOBLIN code by Yamagishi [22] using elaborate magnetic data from which the numerical values used in *S-B* and *I-B* are taken.

In order to examine the relevance of  $q$  and  $\hat{s}$  in the growth rates, the *S-B* and *I-B*

configurations with  $q = 1.5$  and  $\hat{s} = -1$  are also displayed in the right hand-side plot of Fig.2. It can be seen that they are indeed closer to each other than in the  $S-A$  and  $I-A$  cases but not as much as the implementations with safety factor and shear taken from the accurate magnetic data. Therefore, the destabilization of the ITG modes is influenced not only by the introduction of the side-band terms on the expansion of  $\mathbf{B}$  on a magnetic surface but also by  $q$  and  $\hat{s}$ , which alter the profiles of the curvature and the ITG-mode eigenfunction along the field line [23].

These linear results predict that the inward shifted scenario will trigger a more rapid initial growth of ITG modes than the standard case although the difference is greatly reduced when realistic parameters are considered. Recent nonlinear simulation results by Watanabe [10] for the ITG turbulence in helical systems described by the parameters of  $S-A$  and  $I-A$  show that the initial difference in growth rates between the single and multiple configurations triggers a higher AT level for the latter case. Nevertheless, regulation of the ITG turbulence associated with the generation of ZF reduces the difference in the turbulent ion thermal diffusivities for the two cases to comparable levels. It is conjectured that the higher response of the ZF to the turbulent source is responsible for the greater regulation of the AT in the inward-shifted configuration. Linear ZF simulations leading to this discussion are presented in the next section.

#### IV. ZONAL FLOW EVOLUTION

The ZF theory states that its evolution is determined by the convolution of two main factors: a source term related to the  $\mathbf{E} \times \mathbf{B}$  non-linearity and a response function, or kernel  $K(t) = \phi(t)/\phi(0)$  (with  $\phi(t) = \phi_{k_x}(t)$  being the electrostatic potential), which governs the time evolution of the ZF in response to a given initial perturbation. This kernel consists of a rapidly-varying part dominated by the GAM oscillations ( $\mathcal{K}_{GAM}(t)$ ) and a slowly-varying part ( $\mathcal{K}_L(t)$ ) which characterizes the long time response of the kernel [9]. In this section, simulation results for the response kernel in the different model configurations described in Sec. II are shown, together with a comparison with the analytical theory. A discussion of the relationship between NCT optimization and higher ZF level is then given through the velocity-space studies of the realistic model cases ( $S-B$  and  $I-B$ ).

##### A. Simulation results

In the present subsection, linear gyrokinetic simulations with the GKV code of the ZF component for both sets of implementations described in Sec. II are presented. The simulation results are shown in Fig.3, where the numerical values of the previous section are used except that now  $k_y \rho_{ti} = 0$ . The values used for the radial wave number are  $k_x \rho_{ti} = 0.096$  for both the  $S-A$  and  $I-A$  cases and  $k_y \rho_{ti} = 0.103$  and  $0.104$  for the  $S-B$  and  $I-B$  configurations, respectively. These small difference between the values  $k_y \rho_{ti}$  have a negligible effect on the results presented here. Note that the same units for the time variable  $L_n/v_{ti}$  as in Sec. III are used. The more relevant units  $R_0/v_{ti}$  are directly obtained by the relation:  $R_0/v_{ti} = (L_n/R_0)(L_n/v_{ti}) = 0.3(L_n/v_{ti})$ . The initial perturbation of the ion distribution function is assumed to be given by  $\delta f(t=0) = \delta n \exp(-m_i v_i^2/2T_i)$ . In Fig.3, the ZF evolution for the  $S-A$  and  $I-A$  cases is displayed in the top plot while the more realistic  $S-B$  and  $I-B$  cases are depicted in the bottom plot. Once again, both sets of scenarios show a remarkable difference. It can be seen that there is a clearer contrast in the early ZF level between the  $S-B$  and  $I-B$  configurations than between the  $S-A$  and  $I-A$  cases. Therefore, unlike the ITG growth rates, the discrepancy in ZF evolution for standard and

inward-shifted LHD configurations seems to be greater when realistic magnetic geometry parameters are used. It is also observed that the lower safety factor in the  $S$ - $A$  and  $I$ - $A$  models imply a faster damping of the GAM oscillations in agreement with global drift kinetic calculations by Satake *et al.*[24] as well as with theoretical predictions [9]. For all implementations, the residual ZF level at  $t \rightarrow \infty$  does not differ much. It is accepted that it is the low frequency (or stationary) and not the high frequency ZF level what provides the main contribution to the reduction of AT [25]. Therefore, the correlation between the AT and the linear ZF response should come, not only from the ZF response at  $t \rightarrow \infty$ , but also from the different rate of reduction of the time-averaged response with rapid oscillation (such as the GAM) disregarded. Thus, we define the ‘‘ZF decay time’’ as:

$$\tau_{ZF} \equiv \int_0^{t_f} dt \frac{\langle \phi(t) \rangle}{\langle \phi(0) \rangle} \approx \int_0^{t_f} dt \mathcal{K}_L(t), \quad (5)$$

where  $t_f$  represents the time in which the residual ZF level is achieved or does not change significantly for the purpose of the comparison between configurations. In the simulation, the GAM-averaged response kernel, denoted as  $\mathcal{K}_L^{num}(t)$ , is calculated as follows:

$$\mathcal{K}_L^{num}(t) = \frac{1}{T_{GAM}} \int_{t-T_{GAM}/2}^{t+T_{GAM}/2} \langle \phi(t') \rangle / \langle \phi(0) \rangle dt', \quad \text{for } t \geq T_{GAM}/2, \quad (6)$$

where  $T_{GAM}$  is the period of the GAM oscillations. For  $t < T_{GAM}/2$ , numerical extrapolation has been carried out. The GAM-averaged profiles correspond to the slowly-varying curves in Fig. 3. Comparing  $\tau_{ZF}$  for  $t_f = 80[L_n/v_{ti}]$  in both sets of scenarios it can be seen that the  $I$ - $B$  ZF decay time ( $\tau_{ZF}^{I-B} = 5.6[L_n/v_{ti}] = 18.7[R_0/v_{ti}]$ ) is around 65% greater than in the  $S$ - $B$  case ( $\tau_{ZF}^{S-B} = 3.4[L_n/v_{ti}] = 11.3[R_0/v_{ti}]$ ), while in  $I$ - $A$  ( $\tau_{ZF}^{I-A} = 4.0[L_n/v_{ti}] = 13.3[R_0/v_{ti}]$ ) is 38% greater than in the  $S$ - $A$  case ( $\tau_{ZF}^{S-A} = 2.9[L_n/v_{ti}] = 9.7[R_0/v_{ti}]$ ).

It has been argued in [9, 10] that NCT optimization leads to a lower radial drift of helically trapped particles and therefore keeps a high ZF level for a longer time. The constant value of the magnetic field strength of the bottoms of the ripples in the overall magnetic profile for the  $I$ - $B$  and  $I$ - $A$  configurations (see Fig.1) suggests a reduction of the radial drift velocity of the particles deeply trapped in helical ripples. Accordingly, longer ZF decay times are expected for the inward shifted configuration models ( $I$ - $A$  and  $I$ - $B$ ) than for the standard models ( $S$ - $A$  and  $S$ - $B$ ). The question is, why is the improvement of the ZF decay time greater for the realistic inward shift model ( $I$ - $B$ ) than for the simple model ( $I$ - $A$ )? In order to answer this question, in the next section a comparison of the simulation results with the analytical theory predictions for the linear response of the ZF in multiple-helicity systems [9] is presented .

## B. Comparison with analytical predictions

The linear collisionless theory for the dynamics of ZFs is modeled by the following equations [9]:

$$\phi_{k_\perp}(t) = \mathcal{K}(t)\phi_{k_\perp}(0), \quad \mathcal{K}(t) = \mathcal{K}_{GAM}(t)[1 - \mathcal{K}_L(0)] + \mathcal{K}_L(t), \quad (7)$$

$$\mathcal{K}_L(t) = \frac{1 - (2/\pi) \langle (2\epsilon_H)^{1/2} (1 - g_{1i}(t, \theta)) \rangle}{1 + G + \frac{\mathcal{E}(t)}{(n_0 \langle k_\perp^2 \rho_{ti}^2 \rangle)}}, \quad (8)$$

where  $\langle \dots \rangle$  denotes flux surface average (which, in this analysis, is approximated to the poloidal angle average  $(2\pi)^{-1} \oint \dots d\theta$ , as stated in [9]).  $\mathcal{K}_{GAM}(t)$  refers to the analytical description of the GAM oscillations  $\mathcal{K}_{GAM}(t) = \cos(\omega_r t) \exp(-\gamma t)$  and  $\mathcal{K}_L(t)$  is the non-oscillatory long time response kernel.  $\mathcal{E}(t)$  accounts for the additional shielding caused by the radial drift of non-adiabatic helically trapped particles [9] and can be expressed as:

$$\mathcal{E}(t) = \frac{2}{\pi} n_0 \left[ \langle (2\epsilon_H)^{1/2} \{1 - g_{i1}(t, \theta)\} \rangle - \frac{3}{2} \langle k_{\perp}^2 \rho_{ti}^2 \rangle \langle (2\epsilon_H)^{1/2} \{1 - g_{i2}(t, \theta)\} \rangle \right], \quad (9)$$

where the electron contribution is ignored. The functions  $g_{i1}(t, \theta)$  and  $g_{i2}(t, \theta)$  are such that  $g_{i1} = g_{i2} = 1$  at  $t = 0$  giving  $\mathcal{E}(t = 0) = 0$  (*i.e.*, there is no shielding before the helically trapped particles begin to experience the radial drift) and  $g_{i1} = g_{i2} \simeq 0$  at  $t \gg \tau_c = 1/(k_r v_{dr})$ , where  $\tau_c$  denotes as the characteristic time for the shielding.

The analytical derivation of the kernel  $\mathcal{K}(t)$  in the right hand-side equation in (7) clearly differentiates two parts. The first part, corresponding to the earlier stages of the evolution, is dominated by the GAM oscillations. The second part, however, is governed by the long time kernel  $\mathcal{K}_L(t)$ . The collisionless long-time limit of this kernel gives the so-called residual level.  $\mathcal{K}_L(t)$  is also responsible for the non-oscillatory (or time-averaged) ZF in the early stages. Correspondingly, the limiting values of the kernel take the following shape:

$$\mathcal{K}_{<} \equiv \lim_{t \rightarrow 0} \mathcal{K}_L(t) = \frac{1}{1 + G} \quad (10)$$

$$\mathcal{K}_{>} \equiv \lim_{t \rightarrow \infty} \mathcal{K}_L(t) = \frac{\langle k^2 \rho_{ti}^2 \rangle [1 - (2/\pi) \langle (2\epsilon_H)^{1/2} \rangle]}{\langle k^2 \rho_{ti}^2 \rangle [1 - (3/\pi) \langle (2\epsilon_H)^{1/2} \rangle + G] + (2/\pi) \langle (2\epsilon_H)^{1/2} \rangle}. \quad (11)$$

Equation (10) shows that, for  $t < \tau_c$ , the ZF response is governed by the shielding due to the toroidally trapped ions. Here,  $G$  represents the ratio of the neoclassical polarization due to toroidally trapped ions to the classical polarization [8] and it is given by:

$$G = \frac{12}{\pi^3} B_0 R_0^2 q^2 \left\langle \frac{B^2}{|\nabla\psi|^2} \right\rangle \left( \int_0^{1/B_M} d\lambda \oint \frac{d\theta}{2\pi} (2\lambda B_0 \epsilon_H)^{-1/2} \kappa^{-1} K(\kappa^{-1}) \right. \\ \times \left. \left\{ (2\lambda B_0 \epsilon_H)^{1/2} \kappa E(\kappa^{-1}) - \frac{\oint (d\theta/2\pi) K(\kappa^{-1}) E(\kappa^{-1})}{\oint (d\theta/2\pi) (2\lambda B_0 \epsilon_H)^{-1/2} \kappa^{-1} K(\kappa^{-1})} \right\}^2 \right. \\ \left. + \int_{1/B_M}^{1/B_{M'}} d\lambda \int_{\kappa^2(\theta) > 1} \frac{d\theta}{2\pi} (2\lambda B_0 \epsilon_H)^{1/2} \kappa K(\kappa^{-1}) \left\{ E(\kappa^{-1}) - \frac{1}{\kappa} \left( \frac{\epsilon_H(\theta_t)}{\epsilon_H} \right)^{1/2} \right\}^2 \right), \quad (12)$$

where the dependence on the magnetic structure is included in  $\epsilon_H(\theta)$  which accounts for the multiple helicity effects.  $\theta_t(\lambda)$  defines the boundary between helically and toroidally trapped particles and  $E(\kappa)$  and  $K(\kappa)$  are the complete elliptic integrals. In the tokamak limit ( $\epsilon_H \rightarrow 0$ ), we have  $G = 1.6 q^2 / \sqrt{\epsilon_t}$  and  $\mathcal{K}_{>} = \mathcal{K}_{<} = 1/(1 + 1.6 q^2 / \sqrt{\epsilon_t})$  which give the Rosenbluth-Hinton residual level. Following [8] we define the trapping parameter  $\kappa$  as:

$$\kappa^2 = \frac{1 - \lambda B_0 (1 - \epsilon_T(\theta) - \epsilon_H(\theta))}{2\lambda B_0 \epsilon_H(\theta)}, \quad (13)$$

where  $\lambda \equiv \mu/w = (v_\perp/v)^2/B$  with  $\mu$  and  $w$  being the magnetic moment and the kinetic energy, respectively. Thus, we say that particles are either passing or toroidally trapped if they fall within the region  $\kappa^2 > 1$  and they are helically trapped if  $\kappa^2 < 1$ , therefore the boundary is given by the condition  $\kappa^2 = 1$  which defines  $\theta_t$ .  $\psi$  represents the toroidal magnetic flux and the radial coordinate  $r$  is defined by  $\psi = B_0 r^2/2$  (see Ref. [9]). It is then possible to calculate  $G$  and consequently the limiting values of the kernel. In order to calculate the evolution of the kernel between these limiting values, however, it is necessary to take into account the shape of the functions  $g_{i1}$  and  $g_{i2}$  in Eq. (8) (see Ref. [9] for a detailed definition) which depend mainly on the relation:  $k_r V_{dr} t$ . In Ref. [9] the bounce-averaged radial drift velocity  $V_{dr}$  at  $v = v_{Ti} = \sqrt{2}v_{ti} = \sqrt{2T_i/m_i}$  is taken to be:

$$V_{dr}(\theta, \kappa) = \frac{cT_i}{e\psi'} \left[ \frac{\partial \epsilon_H}{\partial \theta} \left( 2 \frac{E(\kappa)}{K(\kappa)} - 1 \right) + \frac{\partial \epsilon_T}{\partial \theta} \right]. \quad (14)$$

We are now in the position of visualizing the complete time evolution of  $\mathcal{K}_L$ . In Fig. 4, the analytical profiles and the ones corresponding to the numerical average of the simulations are presented. Naturally, the oscillation-averaged profiles obtained using Eq. (6) have to be extrapolated to  $t = 0$  and can not depict the detailed shape of the functions calculated in the analytical case. In addition, there seems to be an overall overestimation of  $\mathcal{K}_L$  in the analytical case, as seen already in Ref. [9] due to the approximations assumed for the analytical implementation. Nevertheless, the similarity of the profiles is evident which motivates the use of the analytical implementations to study in more detail the reasons of the discrepancy between ZF evolution in the simple and realistic models for standard and inward-shifted configurations.

The analytical values of  $\mathcal{K}_>$  and the ones from the simulation at  $t = 80[L_n/v_{ti}]$  are presented in Table II. In agreement with the theoretical predictions in Ref. [9], the analytical and numerical values are closer in the standard configurations (*S-A* and *S-B*) than in the inward-shifted ones (*I-A* and *I-B*) since the theory is based on the small helical ripple amplitude ( $\epsilon_H$ ) approximation.

Next, we investigate the configuration dependence of the bounce-averaged radial drift velocity  $V_{dr}(\theta, \kappa)$  as defined in Eq. (14). In this equation, there is no explicit dependence on the safety factor. The  $\kappa$ -averaged  $V_{dr}(\theta)$  profiles in the helically trapped region ( $\kappa^2 < 1$ ) are displayed in Fig. 5. In average, the particles in the *I-B* configuration are the ones that have the slowest radial drift. Then, in increasing order of magnitude of  $v_{dr}$ , we have the *I-A*, the *S-B* and finally the *S-A* configurations. This suggests that the magnetic geometry of the *I-B* scenario is the one with the highest NCT optimization. However, it does not explain why the early-time value of the response kernel of the *I-B* case is so different from the one of the *S-B* case, or why the early-time values of  $\mathcal{K}_L(t)$  for *S-A* and *I-A* are so close to each other and in between those of the *S-B* and *I-B* cases. While the  $V_{dr}$  governs the speed with which the ZF decreases due to the shielding effect of helically trapped particles, the initial value of the ZF response,  $\mathcal{K}_<$  or  $\mathcal{K}_L^{num}(t = 0)$  is determined by the shielding effect of the toroidally trapped particles, which is evaluated by  $G$  in Eq. (12). This equation shows that, while the values of  $\epsilon_t$ ,  $\epsilon_h$ ,  $\epsilon_+$  and  $\epsilon_-$  are implicitly modifying the function, another contribution to  $G$  comes from the safety factor  $q$  and the aspect ratio  $r/R_0$  [where the dependence on  $r$  is included through  $|\nabla\psi| = B_0 r$  in Eq. (12)]. In the *S-A* and *I-A* model configurations,  $r/R_0 = \epsilon_t$  is assumed, while in the more realistic models *S-B* and *I-B* the discrepancy between  $r/R_0$  and  $\epsilon_t$  is introduced through the new

parameter  $R\epsilon_t/r$ , as shown in Table I. The introduction of this new parameter permits the discrimination of the effect of the inward plasma shift on  $G$ . Reducing  $R_0$  in the  $I$ - $B$  configuration decreases  $G$  and, therefore, increases  $\mathcal{K}_<$ , by reducing the banana bounce period and the widths of the toroidal banana orbits. The differences in  $q$  also affect considerably  $G$  by changing the orbit widths and, together with  $\epsilon_h$ ,  $\epsilon_+$  and  $\epsilon_-$ , give the final ordering to the values of  $\mathcal{K}_<$  for the different scenarios. These results indicate, once more, the need of an accurate description of the global magnetic configuration in order to efficiently model the shifted LHD configurations.

This subsection has been devoted to the explanation of the configuration dependence of the linear ZF response based on the analytical formulae in Ref. [9]. To verify the validity of the analytical treatment of helically trapped particles, a velocity-space study of the  $I$ - $B$  and  $S$ - $B$  configurations is presented in the next subsection.

### C. Velocity-space studies

The analytical description of the perturbed distribution function (see Ref. [9]) predicts an oscillatory profile of the helically trapped particle distribution in the velocity space which has a periodic dependence on the dimensionless perpendicular velocity  $v_\perp/v_{ti}$  with the velocity-space wave length  $\lambda_v \propto 1/\sqrt{|k_r V_{dr} t|}$ . In order to visualize the effect of the inward plasma shift, the velocity-space structures of the perturbed ion distribution function for the standard,  $S$ - $B$ , and inward,  $I$ - $B$ , configurations are displayed in Fig.6. The left hand side figures correspond to the  $S$ - $B$  configuration and the right hand side ones to the  $I$ - $B$  case, all taken at  $t = 60[L_n/v_{ti}]$ . Here, the values for time and  $\theta$  position have been chosen to help visualizing the periodicity in velocity space predicted by the theory. At  $\theta = 0$  (top row of Fig.6) the magnetic drift is tangential to the magnetic flux surface, so the structures for both configurations are very similar. However, for  $\theta \neq 0$  the radial drift of particles produces blue hollow areas in the helically-trapped particles region of the velocity space. At fixed  $t$  and  $k_\perp$ , being  $v_{dr}$  greater in the  $S$ - $B$  case, its  $\lambda_v$  is shorter so we can visualize a red region of positive ion population after a blue hollow area. Taking the velocity-space integral of this oscillatory distribution profile yields smaller ZF potentials for the standard configurations through the quasineutrality condition. The lower periodicity (or longer  $\lambda_v$ ) of the  $I$ - $B$  case due to the lower drift velocity does not permit the next maximum of the oscillation to be seen. For shorter times, only a hollow area would be discerned in  $S$ - $B$ . This agrees with the theoretical prediction about the behavior of the helically trapped particle distribution.

Thus, the link between lower radial drift of helical ripple trapped particles and higher ZF level has been confirmed by comparison between the analytical predictions and the numerical results for both the ZF time evolution and the velocity-space structures of the perturbed distribution function.

## V. CONCLUSIONS

Linear gyrokinetic simulations with the GKV code have been carried out to investigate effects of the inward plasma shift on the ITG instability and on the ZF evolution in the LHD.

Two sets of parameters to model the standard and the inward shifted configurations have been considered. The first set uses single and multiple helicity fields to model the standard and inward-shifted configurations, respectively, although both use the same

safety factor, the same aspect ratio and a large-aspect-ratio field approximation to evaluate the radial derivative of the field strength. In order to model the inward shift we have introduced side-band helicity terms to reduce the NCT. In the second set, the same configurations are modeled using more realistic values for the safety factor, the aspect ratio, the multiple helicity components and their radial derivatives taken from elaborate field calculations.

The ITG growth rates for the realistic models of both LHD configurations turn out to be closer to each other than in the case of using the simple models. Also, the discrepancy in the ZF time evolution between the *I-B* and *S-B* cases is more evident when using the realistic model parameters. For the simple model parameters, the ZF decay time [defined by Eq. (5)] for the inward-shifted case is 38% larger than for the standard case. However, a 65% increase is achieved when realistic parameters are used.

Analytical predictions of the linear zonal flow response have been shown to be in a qualitative agreement with the simulation. While the radial drift velocity of helically trapped particles is mainly affected by the side-band terms, the early-time behavior of the response depends on an accurate choice of the field strength spectra, the aspect ratio and the safety factor which affect the shielding due to toroidally trapped particles' polarization. Moreover, the slight reduction of the aspect ratio produced by the inward shift has been shown to be one of the main parameters responsible for the enhancement of the difference between the early-time ZF level of the realistic parameter models.

In addition, the velocity-space structures of the perturbed ion distribution function associated with the ZF evolution are examined by the simulation of the standard and inward-shifted configurations *S-B* and *I-B*. As expected from the theory, the fast radial drift of helically trapped particles in the standard case produces an oscillatory distribution and shows hollow and banded regions that lead to a reduction of the ZF when the velocity-space integration of the distribution function is carried out to determine the ZF potential through the quasineutrality condition. Moreover, a periodicity on the velocity-space structures in the helically trapped region has been identified in agreement with the analytical predictions.

More conclusive evidence of the effect of the inward plasma shift on the AT requires very computer-demanding nonlinear turbulence simulations. The present work, however, helps to choose conditions in which high ZF generation by the turbulence is expected. In particular, the results presented here for the standard and inward-shifted configurations are in agreement with recent nonlinear simulation results of the AT [10] which used the simple version of the field models (*S-A* and *I-A*). The larger ITG growth rates of the inward-shifted case (*I-A*) trigger a greater drive of AT while the higher ZF level for this configuration reduces the AT to a comparable level with the standard case (*S-A*). Following the same reasoning, the more realistic set-up (*S-B*, *I-B*) which shows similar ITG destabilization but much greater ZF level should show a greater compensation of the AT in the inward-shifted scenario as it is observed in the experiment. These nonlinear calculations are presently being performed.

## Acknowledgments

The authors would like to thank Dr. O. Yamagishi and Dr. S. Satake for useful information on linear ITG mode behavior in realistic LHD experimental scenarios and fruitful discussion on GAM evolution in helical systems.

This work is supported in part by the Japanese Ministry of Education, Culture, Sports, Science and Technology, Grant Nos. 17-05373, 16560727 and 17360445 and in part by the NIFS Collaborative Research Program, NIFS06KDAD006, NIFS06KNXN060 and NIFS06KTAT038.

- 
- [1] H. E. Mynick, *Phys. Plasmas* **13**, 058102 (2006).
  - [2] D. A. Spong, *Phys. Plasmas* **12**, 056144 (2005).
  - [3] J. N. Talmadge, V. Sakaguchi, F. S. B. Anderson, *et al.*, *Phys. Plasmas* **9**, 5165 (2001).
  - [4] C. Beidler, G. Grieger, F. Herrnagger, *et al.*, *Fusion Technol.* **17**, 148 (1990).
  - [5] G. H. Neilson, M. C. Zarnstorff, J. F. Lyon, *et al.*, *J. of Plasma Fusion Res.* **78**, 214 (2002).
  - [6] D. A. Spong, S. P. Hirshman, L. A. Berry, *et al.*, *Nucl. Fusion* **41**, 711 (2001).
  - [7] H. Yamada, A. Komori, N. Ohyabu *et al.*, *Plasma Phys. Controlled Fusion* **43**, A55 (2001).
  - [8] H. Sugama and T.-H. Watanabe, *Phys. Rev. Lett.* **94**, 115001 (2005).
  - [9] H. Sugama and T.-H. Watanabe, *Phys. Plasmas* **13**, 012501 (2006).
  - [10] T.-H. Watanabe, H. Sugama and S. Ferrando-Margalet, *Proc. 21st IAEA Fusion Energy Conf.*, EX/5-4, 2005 (submitted to Nucl. Fusion)
  - [11] P. H. Diamond, S.-I. Itoh, K. Itoh and T. S. Hahm, *Plasma Phys. Controlled Fusion* **47**, R35 (2005).
  - [12] K. Itoh, S.-I. Itoh, P. H. Diamond, *et al.*, *Phys. Plasmas* **13**, 055502 (2006).
  - [13] A. Fujisawa, K. Itoh, H. Iguchi, *et al.*, *Phys. Rev. Lett.* **93**, 165002 (2004).
  - [14] M. N. Rosenbluth and F. L. Hinton, *Phys. Rev. Lett.* **80**, 724 (1998).
  - [15] O. Motojima, N. Ohyabu, A. Komori *et al.*, *Nucl. Fusion* **43**, 1674 (2003).
  - [16] S. Murakami, A. Wakasa, H. Maassberg, *et al.*, *Nucl. Fusion* **41**, L19-L22 (2002).
  - [17] T.-H. Watanabe and H. Sugama, *Nucl. Fusion* **46**, 24 (2006).
  - [18] E. A. Frieman and L. Chen, *Phys. Fluids* **25**, 502 (1982).
  - [19] H. Sugama and T.-H. Watanabe, *Phys. Plasmas* **11**, 3068 (2004).
  - [20] M. A. Beer, S. C. Cowley and G. W. Hammet, *Phys. Plasmas* **2**, 2687 (1995).
  - [21] T. Kuroda and H. Sugama, *J. Phys. Soc. Jpn.* **70**, 2235 (2001).
  - [22] O. Yamagishi, M. Yokoyama, N. Nakajima, *et al.*, *Phys. Plasmas* **14**, 012505 (2007).
  - [23] T. Kuroda, H. Sugama, R. Kanno, *et al.*, *J. Phys. Soc. Jpn.* **69**, 2485 (2000).
  - [24] S. Satake, H. Sugama and T.-H. Watanabe, *Proc. 21st IAEA Fusion Energy Conf.*, TH/P2-15, 2005 (submitted to Nucl. Fusion)
  - [25] T. S. Hahm, M. A. Beer, Z. Lin, *et al.*, *Phys. Plasmas* **6**, 922 (1999).

	$q$	$\epsilon_t$	$r/R_0$	$\epsilon_h/\epsilon_t$	$\epsilon_-/\epsilon_t$	$\epsilon_+/\epsilon_t$
<b><i>S-A</i></b>	1.5	0.1	0.1	1	0	0
<b><i>I-A</i></b>	1.5	0.1	0.1	1	-0.8	-0.2
<b><i>S-B</i></b>	1.9	0.087	0.099	0.91	-0.28	0
<b><i>I-B</i></b>	1.7	0.082	0.114	1.2	-0.74	-0.24
	$\hat{s}$	$(r/\epsilon_t) \epsilon'_{00}$	$(r/\epsilon_t) \epsilon'_t$	$(r/\epsilon_t) \epsilon'_h$	$(r/\epsilon_t) \epsilon'_-$	$(r/\epsilon_t) \epsilon'_+$
<b><i>S-A</i></b>	-1	0.25	1	2	0	0
<b><i>I-A</i></b>	-1	0.5	1	2	-0.8	-0.6
<b><i>S-B</i></b>	-0.85	0.22	1.02	1.96	-0.63	0
<b><i>I-B</i></b>	-0.96	0.71	1	2.44	-0.36	-0.61

TABLE I: Numerical values for the expansion parameters of the magnetic field and the curvature factor  $G_c$  in the simple (*S-A* and *I-A*) and realistic (*S-B* and *I-B*) model configurations.

	<b><i>S-A</i></b>	<b><i>S-B</i></b>	<b><i>I-A</i></b>	<b><i>I-B</i></b>
$\mathcal{K}_>^{an}$	$2.2 \cdot 10^{-2}$	$2.7 \cdot 10^{-2}$	$2.5 \cdot 10^{-2}$	$2.6 \cdot 10^{-2}$
$\mathcal{K}_L^{num}(t = 80)$	$(2.2 \pm 0.4) \cdot 10^{-2}$	$(2.3 \pm 1.6) \cdot 10^{-2}$	$(1.8 \pm 0.6) \cdot 10^{-2}$	$(1.7 \pm 0.9) \cdot 10^{-2}$

TABLE II: Compared values for the long time ZF residual level from the analytical theory  $\mathcal{K}_>^{an}$  and the simulation  $\mathcal{K}_L^{num}(t)$  at  $t = 80[L_n/v_{Ti}]$ . In these calculations, accurate values for the radial wave vector are required. The values of  $k_x \rho_{ti}$  for *S-A*, *S-B*, *I-A* and *I-B* are, respectively: 0.096, 0.103, 0.096 and 0.104.

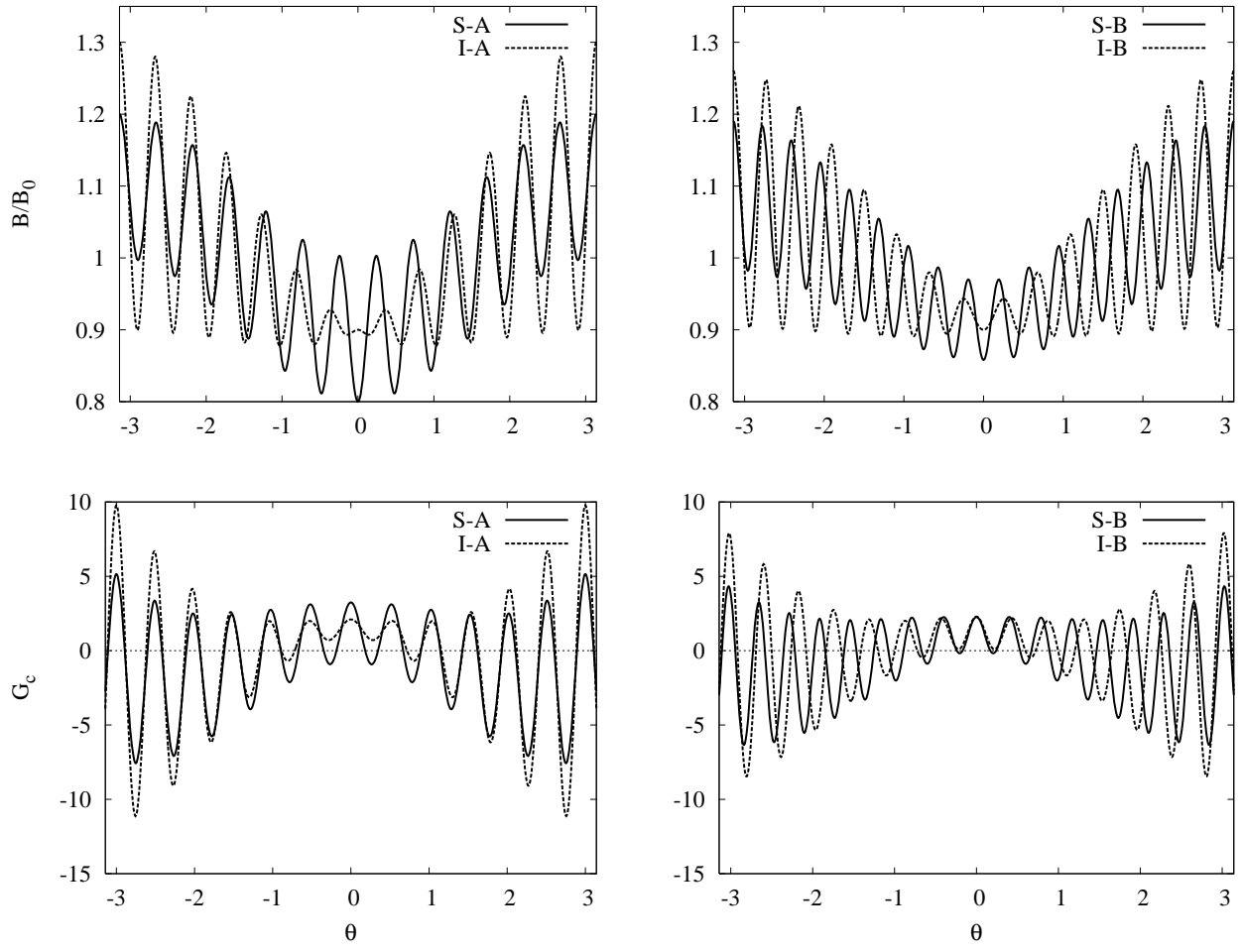


FIG. 1: Magnetic field strength  $B$  and geometric factor  $G_c$  along the magnetic field lines for the simple model configurations  $S$ - $A$  and  $I$ - $A$  (on the left) and the more realistic models  $I$ - $B$  and  $S$ - $B$  (on the right).

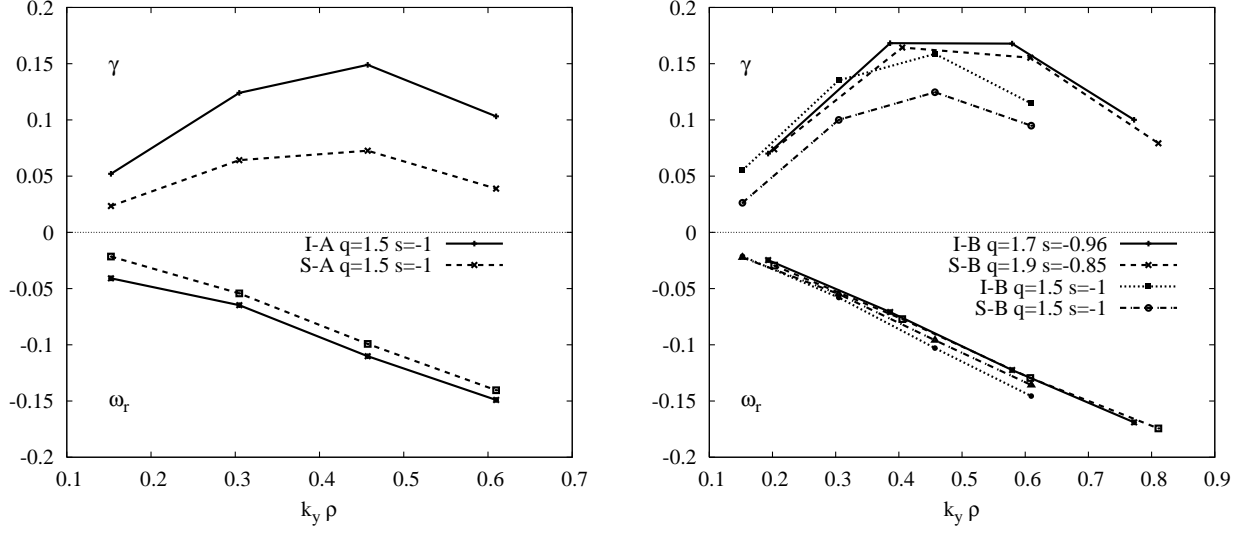


FIG. 2: ITG growth rates and real frequencies (in units of  $v_{ti}/L_n$ ) for the simple model configurations  $S$ - $A$  and  $I$ - $A$  (on the left) and the more realistic models  $I$ - $B$  and  $S$ - $B$  (on the right). The relevance of  $q$  and  $\hat{s}$  is depicted in the right figure for the realistic configurations. Here,  $\rho = \rho_{ti} = \sqrt{v_{ti}/\Omega}$ ,  $L_n/R_0 = 0.3$ ,  $\eta_i = L_n/L_T = 4$ ,  $T_e/T_i = 1$  and  $\alpha = 0$ .

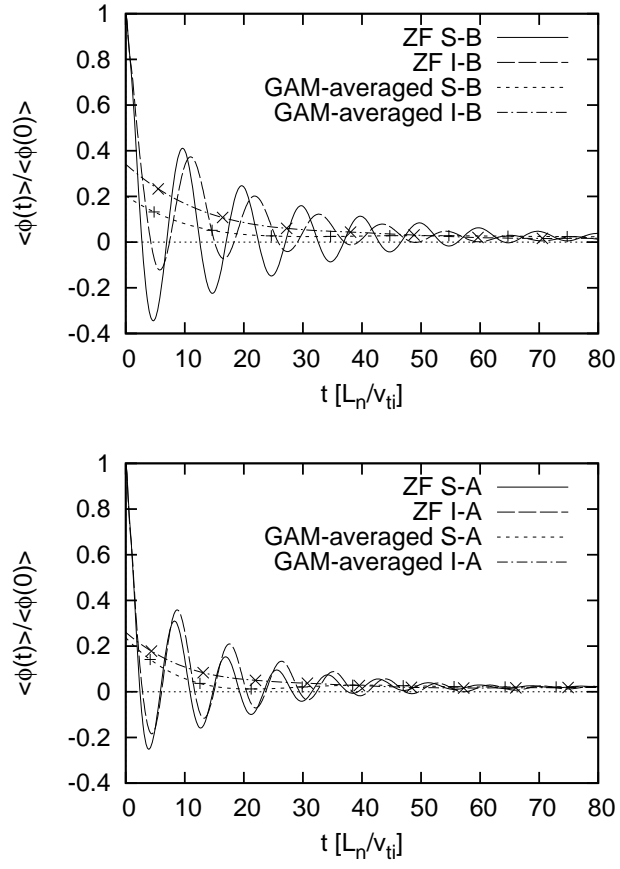


FIG. 3: Compared ZF evolution and GAM-averaged response (as described by Eq. [6]) for the simple (*S-A* and *I-A*, bottom figure) and the realistic (*S-B* and *I-B*, top figure) model configurations, respectively.

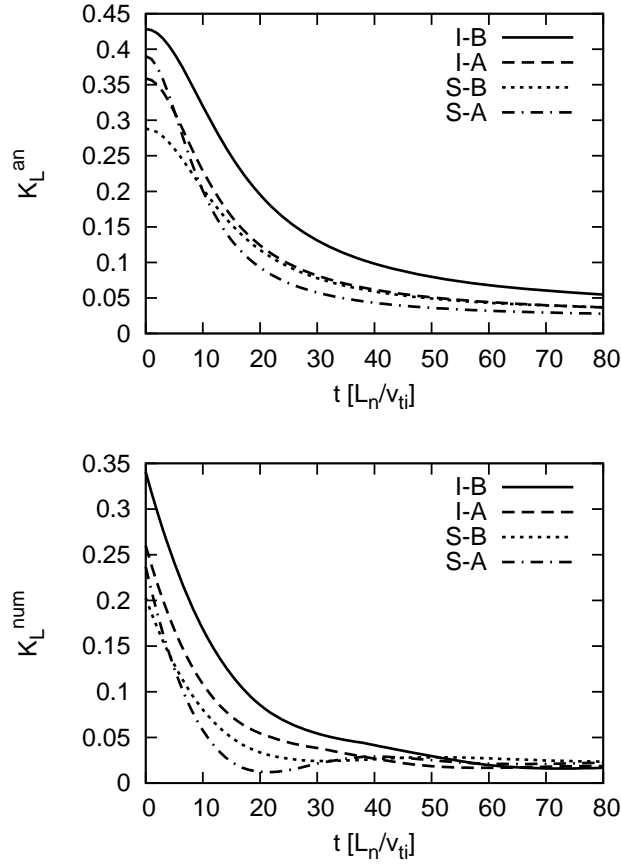


FIG. 4: Analytical profiles  $\mathcal{K}_L^{an}$  (top figure) versus numerical profiles  $\mathcal{K}_L^{num}$  (bottom figure) for the simple (*S-A*, *I-A*) and realistic (*S-B*, *I-B*) model configurations.

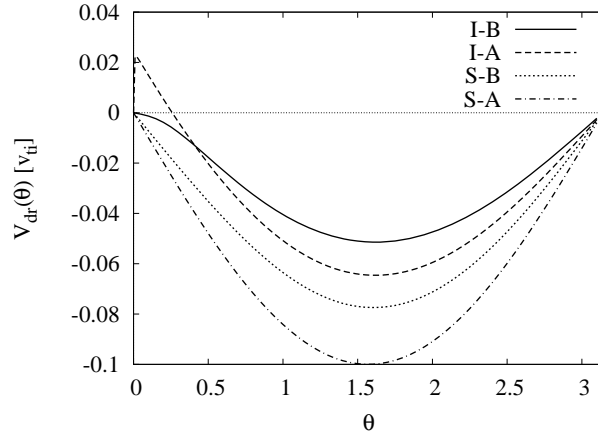


FIG. 5:  $\kappa$ -averaged radial drift velocity profiles for the simple (*S-A*, *I-A*) and realistic (*S-B*, *I-B*) model configurations in the range  $0 < \theta < \pi$ . Note that  $V_{dr}(\theta)$  for  $-\pi < \theta < 0$  is given by  $V_{dr}(-\theta) = -V_{dr}(\theta)$ .

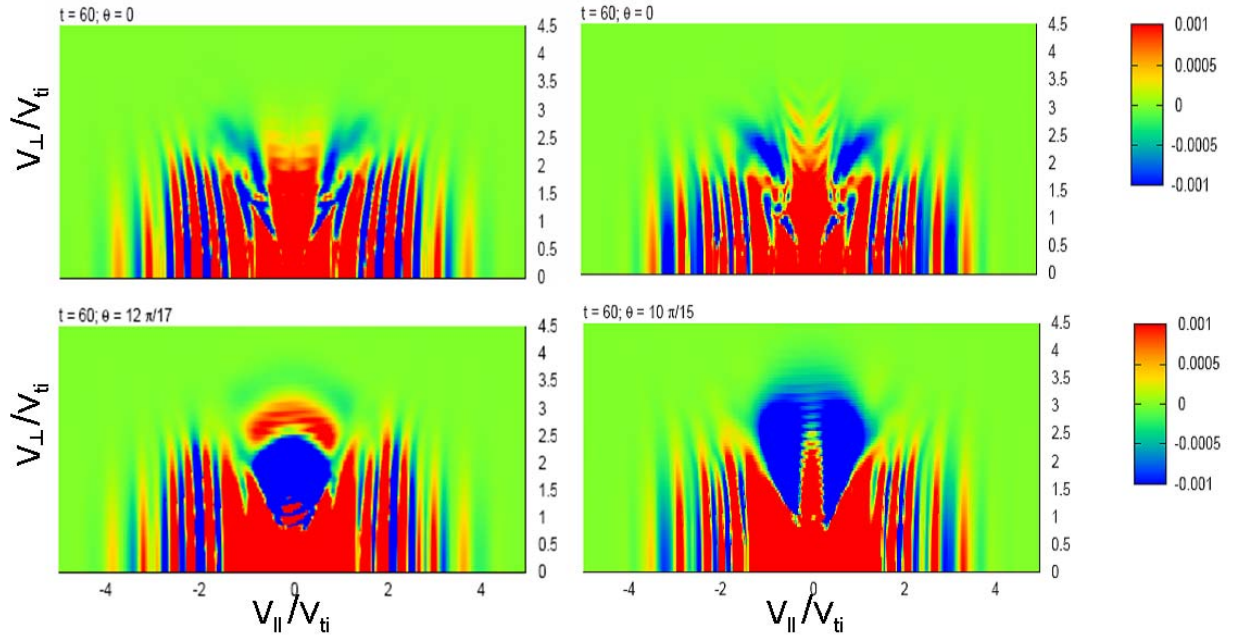


FIG. 6: Compared velocity-space structures for the realistic model standard (*S-B*) (left hand side figures) and inward-shifted (*I-B*) (right hand side figures). The top row corresponds to  $\theta = 0$  and the bottom row to  $\theta$  values corresponding of nearby local magnetic field minima of each configuration. These  $\theta$  positions and the time,  $t = 60[L_n/v_{ti}]$ , are chosen to help to visualize the periodicity in velocity space of the distribution function in the helically trapped region as predicted by the theory.